Received: 6 September 2023 | Accepted: 30 May 2024

DOI: 10.1002/nsg.12314

Near Surface Geophysics EAGE EUROPEAN ASSOCIATION OF GEOSCIENTISTS & ENGINEERS

ORIGINAL ARTICLE

Integration of ground geophysical methods to characterize near-surface aquifer zones within an active mine

Sikelela Gomo[1] | **Ndamulelo Mutshafa**[1] | **Jureya Dildar**[1] | **Musa S. D. Manzi**[1] | **Julie E. Bourdeau**[2] | **Bojan Brodic**[1] | **Ian James**[1,3] | **Gordon R. J. Cooper**[1] | **Raymond J. Durrheim**[1]

[1] School of Geosciences, University of the Witwatersrand, Johannesburg, Republic of South Africa

[2] Independent Researcher, Randfontein, South Africa

[3] Southern Geoscience Consultants, Perth, Australia

Correspondence
Sikelela Gomo, School of Geosciences, University of the Witwatersrand, Johannesburg, Private Bag, Wits, 2050, Republic of South Africa.
Email: 1488846@students.wits.ac.za.

Funding information
Department of Science and Innovation, South Africa; National Research Foundation

Abstract

Understanding near-surface groundwater storage, flow patterns, surface and groundwater interactions in mining areas can assist in making mining more efficient and profitable. This is especially important in opencast mines affected by water inflows that may negatively affect production and increase mining costs. We map and characterize the near-surface aquifer zones at the opencast site of Tharisa Minerals, located in the southwestern region of the Bushveld Complex (South Africa). The main goal is to infer pit water inflow at the mine site and determine how it may be better controlled. The Bushveld Complex hosts partially connected and unconfined alluvial, shallow-weathered and crystalline bedrock aquifers, which are often connected by small-scale permeable zones. Seismic refraction tomography, multichannel analysis of surface waves, electrical resistivity tomography and borehole data are used to map and understand the different aquifer zones in the vicinity of the mine, as well as infer their relation to water inflow in the mine pits. The geophysical surveys map the overburden, weathered bedrock aquifer zone, and the top of the crystalline aquifer rock zone reasonably well. They reveal extensive and deep weathering, and possible high hydraulic conductivity in the vicinity of the mine. The results provide a better understanding of the mine's near-surface environment, which could be used to implement effective and targeted dewatering techniques, thus enabling better pit inflow water control to improve mine working conditions and production.

KEYWORDS
aquifer, ERT, MASW, refraction, imaging

INTRODUCTION

The Paleoproterozoic Bushveld Complex in South Africa is renowned for its endowment of platinum group metals (PGMs), hosting 90% of the world's reserves (United States Geological Survey (USGS), 2023). The complex also has extensive reserves of chromium, nickel, vanadium, copper, tin and cobalt (Zientek et al., 2014). Both underground and opencast mining are used to extract these resources. Locally, mines in the Bushveld Complex suffer from inflows of groundwater, which may delay production and increase the complexity and cost of mining operations. Groundwater inflow rates into the mines are highly variable and can be derived from multiple sources. These range from inflows originating from distinct fracture systems drawing on water from both local and distant sources, as well as water flowing from the shallow weathered aquifer zone (Gebrekristos &

Cheshire, 2012; Titus et al., 2009). The structural environment in which mines are located has a considerable impact on the groundwater inflow rates, and this is especially true for surface mines (i.e., opencast mines). In opencast mining, pit flooding commonly occurs when mining levels are below the water table and/or weathered aquifer zone, when rivers and dams overflow, or through constant influx of water into the pits from extensive rainfall. Interestingly, groundwater inflows are principally associated with jointing and small-scale faults rather than large faults, which are often found to be dry (Titus et al., 2009).

To understand the conditions in the top 50–100 m (so-called near-surface) of the crust, different geophysical methods are commonly applied. Among the geophysical methods, seismic refraction tomography (SRT), multichannel analysis of surface waves (MASW) and electrical resistivity tomography (ERT) are very effective in mapping water-bearing strata, conducting site investigations, studying esker architecture and mapping stratigraphic variations (Alcala et al., 2021; Al-Heety et al., 2021; Ali et al., 2021; Brodic et al., 2018; Gomo et al., 2023; Hasan et al., 2021; Malehmir et al., 2018; Salas-Romero et al., 2021; Shankar, 1994). For hydrological purposes, the geophysical methods can delineate aquifers (e.g., porous and permeable fracture zones, buried valleys and karst and volcanic cave aquifers), map groundwater-controlling features and structures that influence aquifers (e.g., salt domes), assess groundwater potential and overburden protective competency of aquifers, and infer groundwater quality, amongst other uses (Akintoriwa & Olowolafe, 2013; Gabriel et al., 2003; Malehmir et al., 2018; Poulsen & Christensen, 1999; Shankar, 1994).

To demonstrate the potential of near-surface geophysical methods for hydrological purposes in opencast mines, we use a combined approach of SRT, MASW, ERT and borehole data to map the near-surface aquifer environment at Tharisa Minerals. Tharisa Minerals is an opencast PGMs and chrome mine situated in the Marikana section, located in the southwestern portion of the Bushveld Complex. Currently, mining at Tharisa Minerals is occurring from surface to depths of about 120 m. The mine is seriously affected by mine fissure inflows. This study aims to: (1) image and characterize the near-surface (top ~35 m) weathered aquifer zone within the vicinity of the mine; (2) evaluate the nature of the overburden to infer surface and groundwater interaction; and (3) determine how pit water inflow control can be improved at the mine. Our results demonstrate that hydrological knowledge gaps can be addressed using geophysical methods, providing valuable insights to mines affected by water fissure inflow.

GEOLOGICAL SETTING OF THE STUDY AREA

The Paleoproterozoic (2.06 Ga) Bushveld Complex is situated in the northeastern part of South Africa (Figure 1a; Cawthorn, 2015). The complex contains the largest continental layered mafic-ultramafic intrusion in the world, called the Rustenburg Layered Suite (RLS), covering an area of approximately 65,000 km^2 and hosts stratiform deposits of PGMs, chromium and vanadium (Boorman et al., 2004; Cawthorn, 2015; Eales & Cawthorn, 1996; Hey, 1999; Scoates et al., 2021). The stratigraphy of the RLS is subdivided into five zones. From bottom to top: (1) Marginal Zone, consisting of poorly-layered norites and pyroxenites; (2) Lower Zone, consisting primarily of harzburgite, pyroxenite and feldspathic pyroxenite; (3) Critical Zone, which is subdivided into the Upper and Lower Critical Zones (based on where cumulus plagioclase first appears), consisting of layered pyroxenite-norite-anorthosite-chromitite sequences; (4) Main Zone, consisting of poorly-layered norite and gabbronorite; and, finally, (5) Upper Zone, which consists of ferrogabbro-anorthosite-magnetitite-, and apatite-bearing diorites (Boorman et al., 2004; Cawthron, 2015; Eales & Cawthron, 1996; Hey, 1999). Spatially, the study area is situated in the southern portion of the western limb of the Bushveld Complex and overlaps rocks from the Lower, Critical and Main Zone (Figure 2b).

RLS rocks are transected by numerous small-scale fractures (faults and joints) related to tectonically controlled geomorphic processes. These discontinuities form complex fracture networks that vary spatially and over time and act as structural groundwater flow controls (Roberts & Clark-Mostert, 2010; Twidale & Romani, 2005; Wilson et al., 2005). The complex fracture networks, combined with weathered and fresh rocks, enable the formation of near-surface bedrock aquifers (intergranular weathered bedrock aquifers) in the weathering zone, as well as deeper (>300 m depth) fractured aquifers (Fourie et al., 2017; Van Wyk, 2013; Govender, 2019). The Bushveld Complex is known to host three types of aquifers: (1) alluvial; (2) shallow weathered bedrock; and (3) a deeper fractured aquifer (Gebrekristos & Cheshire, 2012; Titus et al., 2009). Both the alluvial and shallow bedrock aquifers are within the weathered zone (from surface to about 50 m deep, depending on the locality), whereas the deeper fractured aquifer is located below the weathered zone and extends to depths where fractures have been closed by increased overburden pressure (Lourens, 2013). The alluvial, shallow weathered and deeper fractured aquifers are often connected by structural discontinuities, and, in mining

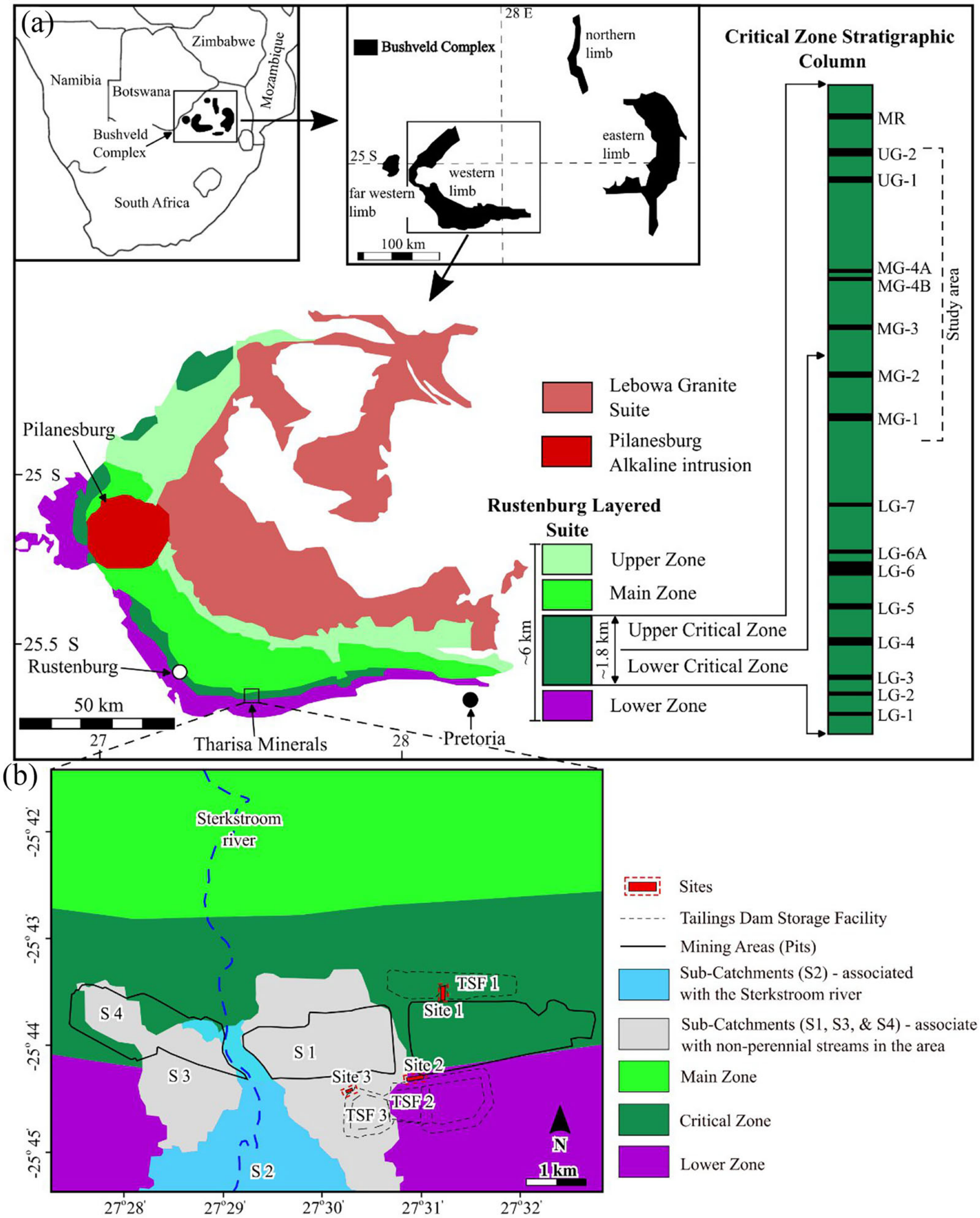

FIGURE 1 Location of the western portion of the Bushveld Complex (South Africa), along with the location of Tharisa Minerals and the stratigraphy of the Critical Zone, in which Tharisa Minerals is situated (modified after Junge et al., 2016). The Critical Zone stratigraphical column shows the chromitite seams of the Lower Group (LG), Middle Group (MG), Upper Group (UG) and Merensky reef (MR). (b) Local geological map of Tharisa Minerals, illustrating the survey areas, pit locations and the location of Sterkstroom River and sub-catchments (Cuthbertson, 2022) located around the mine.

areas, the groundwater flow between them is controlled by mine voids and rapid vertical inflow via the interconnected fracture network and weathered zones (Gebrekristos & Cheshire, 2012; Titus et al., 2009). On a regional scale, weathered aquifers may be connected to river systems, alluvial aquifers and deeper fractured bedrock aquifer systems.

METHODS AND DATA ACQUISITION

High-resolution, active-source SRT, MASW and ERT surveys were conducted to mapthe P- and S-wave velocity, as well as the electrical resistivity distribution in the top 35 m via 2D profiling (Figure 2). Data were acquired at three sites located in the vicinity of the mine, next

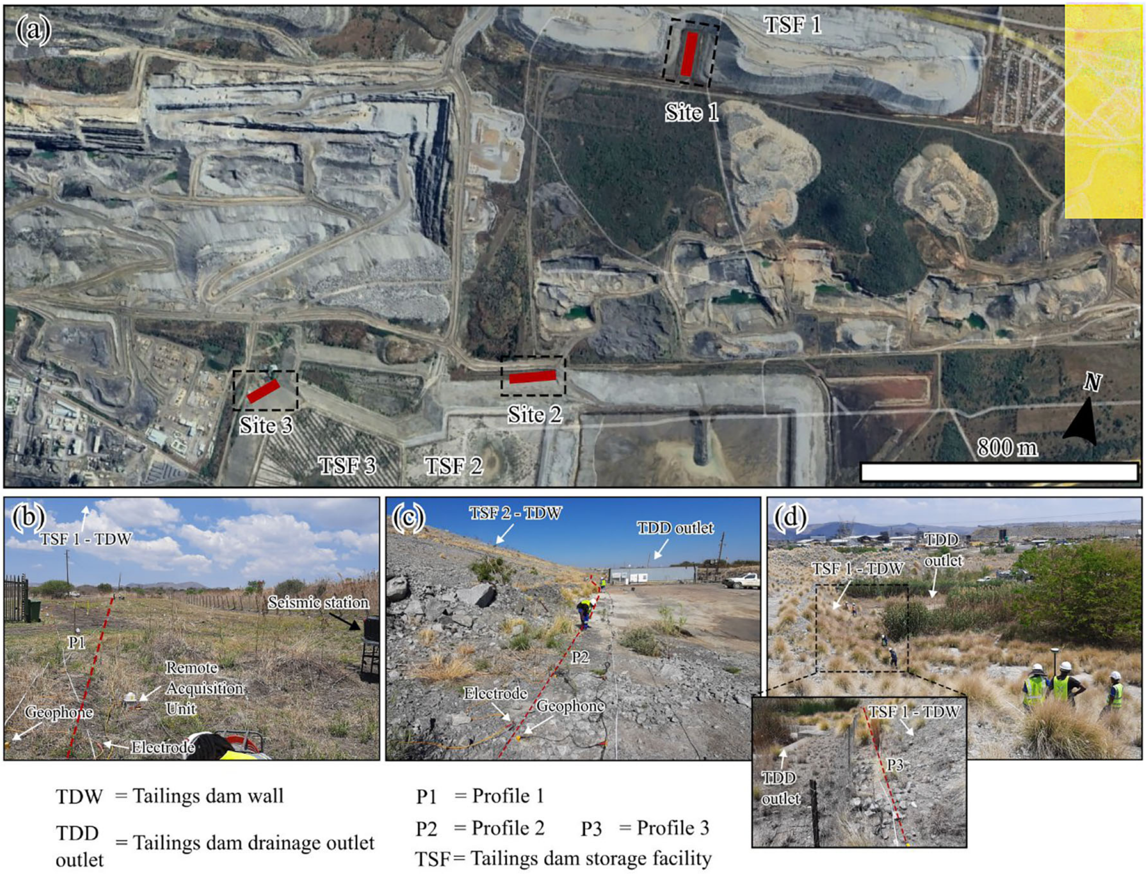

FIGURE 2 (a) Sites 1–3 locations (Google Earth image) at Tharisa Minerals. All the sites are located near tailings dam storage facility tailings storage facilities (TSF) 1, TSF 2 and TSF 3; (b), (c) and (d) show field photos of Sites 1–3, and locations where profiles 1–3 were acquired.

to three different tailings storage facilities (Figure 2a). All profiles (i.e., P1, P2 and P3) were acquired on relatively flat ground (Figure 2b–d). Borehole data (spatially closest-available data) were taken from about 1.5 km west of the study areas and later integrated in the study for interpretation purposes.

Seismic refraction tomography (SRT)

The seismic data used for P-wave first arrival tomography purposes were acquired using a fixed-spread (Site 1) and an end-on acquisition spread (Sites 2 and 3). For all sites, a 6 kg sledgehammer was used as a seismic source striking a 20 × 20 × 2 cm aluminium plate. Five hits were made at each shot point to improve the signal-to-noise ratio. The data were acquired using a sampling interval of 1 ms and a recording length of 1000 ms. At Site 1, the acquisition was carried out using a 48-channel seismograph system with 14 Hz natural frequency vertical component geophones spaced at 4 m intervals. The shots were taken at every receiver location and one offset point, on both sides of the spread. The P-wave tomograms for Sites 2 and 3 were produced from the same datasets acquired for MASW purposes (end-on spread). The MASW data acquisition is presented in the following section and detailed in Table 1. All shot and receiver locations were accurately surveyed using a differential global positioning system (DGPS) with an accuracy of a few centimetres in both the geodetic positioning and elevation.

At all sites, P-wave first breaks were manually picked after adding corresponding geometry to the SEG-Y trace headers. The travel-time tomography inversion was done in TomoPlus, a commercial software that uses a non-linear travel-time inversion method, based on inverting travel-time curves rather than travel-times alone, to deduce the velocity models (Zhang & Toksoz, 1998). Cell sizes of 1 m in both inline and depth directions were used to invert the data. Figure 3a shows an example plot of the travel-time residuals as a function of offset, obtained after 10 iterations, whereas Figure 3b shows an example of the distribution of picked P-wave first arrivals as a function of offset for profile P1. The final P-wave tomograms are shown in Figure 4a,c,e, and their corresponding ray-paths in Figure 4b,d,f. Average root

TABLE 1 Multichannel analysis of surface waves (MASW) and electrical resistivity tomography (ERT) survey acquisition parameters.

MASW parameters	Site 1 – Parameters	Site 2 – Parameters	Site 3 – Parameters
Area	Site 1	Site 2	Site 3
Survey type	Fixed spread roll-along	Fixed spread roll-along	Fixed spread roll-along
Data format	SEG-2	SEG-2	SEG-2
Number of channels	24	24	24
Seismic source	6 kg sledgehammer	6 kg sledgehammer	6 kg sledgehammer
Stack	5 repeated hits per location	5 repeated hits per location	5 repeated hits per location
No. of shot points	17	23	24
Line length	96 m	88 m	46 m
Geophone frequency	14 Hz	14 Hz	14 Hz
Geophone spacing	3 m	2 m	2 m
Roll along spacing	6 m	4 m	2 m
Source offset	21 m	12 m	12 m
Sampling interval	1 ms	1 ms	1 ms
Record length	1000 ms	1000 ms	1000 ms
Geodetic surveying	DGPS	DGPS	DGPS
ERT parameters	**Site 1 – Parameters**	**Site 2 – Parameters**	**Site 3 – Parameters**
Equipment	ARES resistivity metre	ARES resistivity metre	ARES resistivity metre
Electrode spacing (m)	4	2	2
Line length (m)	160	80	80
Array types used to acquire data	Schlumberger, Wenner and Dipole–Dipole	Schlumberger, Wenner and Dipole–Dipole	Schlumberger

Abbreviation: DGPS, differential global positioning system.

mean square errors after 10 iterations were 3.52, 1.09 and 2.96 ms for profiles P1 (Site 1), P2 (Site 2) and P3 (Site 3) data, respectively.

Multichannel analysis of surface waves (MASW)

MASW is a non-invasive seismic technique that uses the dispersive nature of surface waves (Rayleigh waves or Love waves) to map the shear-wave velocity (V_S) variation with depth (Park et al., 1999; Socco & Strobbia, 2004). In this study, a standard MASW roll-along technique was applied to acquire the data using a 24-channel seismograph system. Single component (vertical) geophones with a natural frequency of 14 Hz and varying geophone interval, source-to-receiver offset and roll-along shifts were used to acquire the data (Table 1).

Figure 5a,b illustrates the typical data quality obtained, which includes the presence of noisy channels, non-continuity of events and guided waves. The shot gathers shown in Figure 5a,b were taken from data at Sites 3 and 2, respectively. Figure 6a,f shows typical quality shot gathers acquired at Sites 1 and 3, correspondingly. The acquired field data were subjected to pre-processing involving the muting of first breaks and guided waves and eliminating bad traces (Figure 6b,g) to improve the quality and coherency of phase velocity-frequency spectra (Figure 6c,h). After testing different methods, the phase velocity-frequency spectra (dispersion images) were produced using the phase-shift method (Park et al., 1999). For every shot location, the maximum spectral amplitude deemed to correspond to the fundamental mode was picked to obtain a dispersion curve (Figure 6d,i). In cases where the fundamental mode was not clearly visible due to high ambient noise levels and/or distortions by higher modes, muting of the effects of these noise sources was carried out (Figure 6b,g). The picked dispersion curves were individually inverted to obtain 1D shear-wave (V_S) velocity profiles (Figure 6e,j) underneath the middle point of a geophone spread.

The MASW data processing was done in Surfseis 6++. This software adopts a shear-wave inversion algorithm from Xia et al. (1999), which is based on obtaining shear-wave velocities (S-waves) by inverting the dispersive phase velocity of Rayleigh or Love waves. To invert the data, a 10-layer model with increasing thickness and density with depth was used. The initial densities used changed in an orderly increasing manner with depth and ranged from 1.5 to 2.0 g/cm^3. All the model lay-

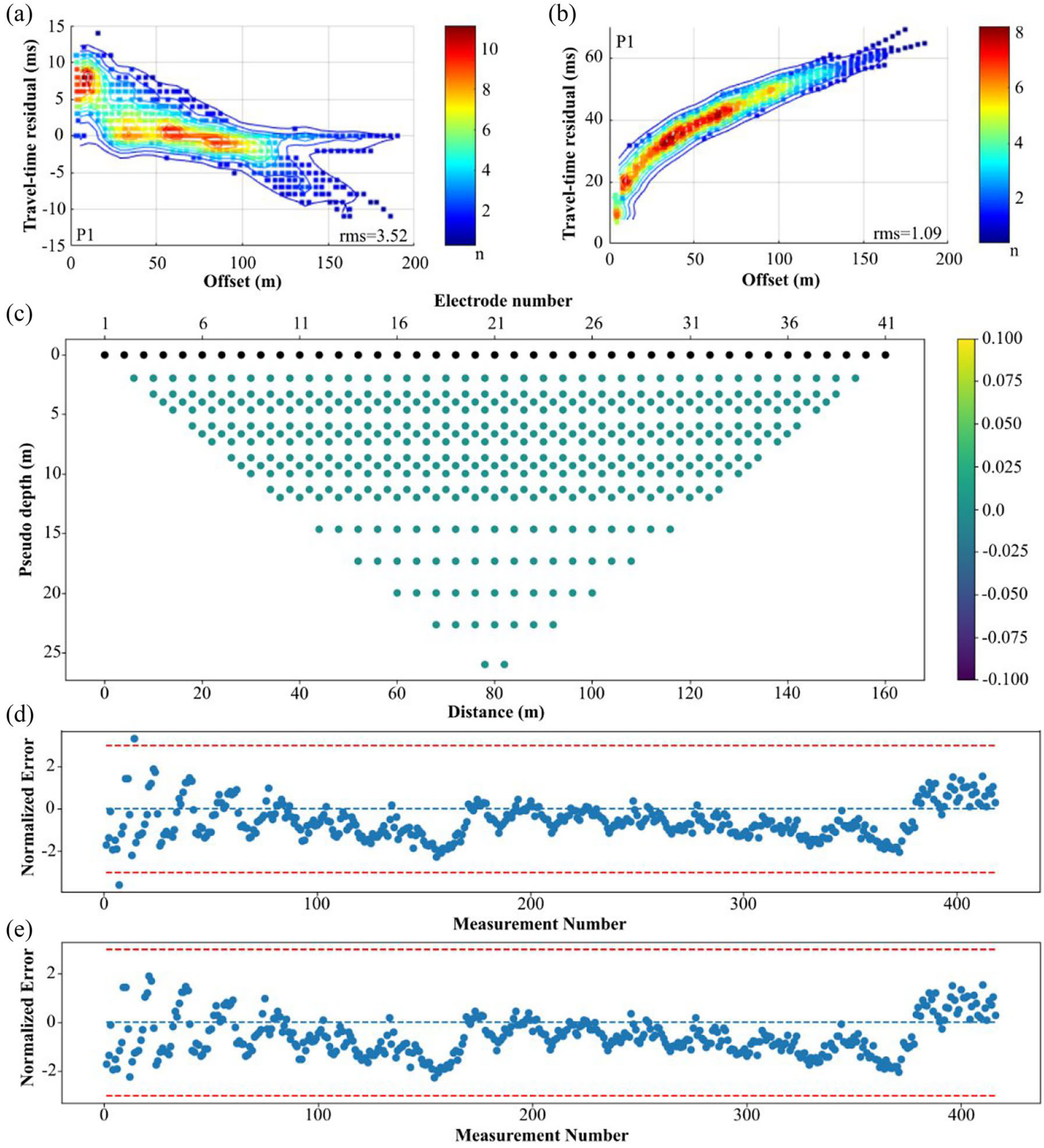

FIGURE 3 Example of seismic and electrical resistivity tomography error assessment plots at Site 1. (a) Travel-time residuals (root mean square misfit) plots obtained after 10 iterations and (b) its corresponding first picked breaks as a function of offset for seismic refraction tomography profile P1 (Site 1). The data density, where 'n' is the number of points inside a range, is represented by the colour scale used to depict the data. (c) Electrical resistivity survey measurement stacking error (Dev.) pseudo section for the Schlumberger array electrical resistivity tomography at Site 1. (d) and (e) Normalized inversion error assessment plots for each data point after an initial resistivity inverse model is calculated.

ers had an initial Poisson's ratio of 0.4. The depth of the half-space used to invert the data was determined from the longest surface wave wavelength measured from the obtained dispersion curves. The inversion algorithm was allowed 10 iterations and an average root-mean-square error of 0.4% was obtained. Using all generated 1D velocity profiles, 2D shear-wave velocity pseudosections were produced by the bicubic interpolation method.

Electrical resistivity tomography (ERT)

Electrical resistivity is a volumetric property of a material that describes its resistance to electrical current flow (Rucker et al., 2009; Telford et al., 1990). For this study, we acquired ERT data using a combination of Schlumberger, Wenner and Dipole–Dipole electrode arrays to obtain good lateral and vertical resolution of the near-surface along the survey traverse. At Site 1, a spread

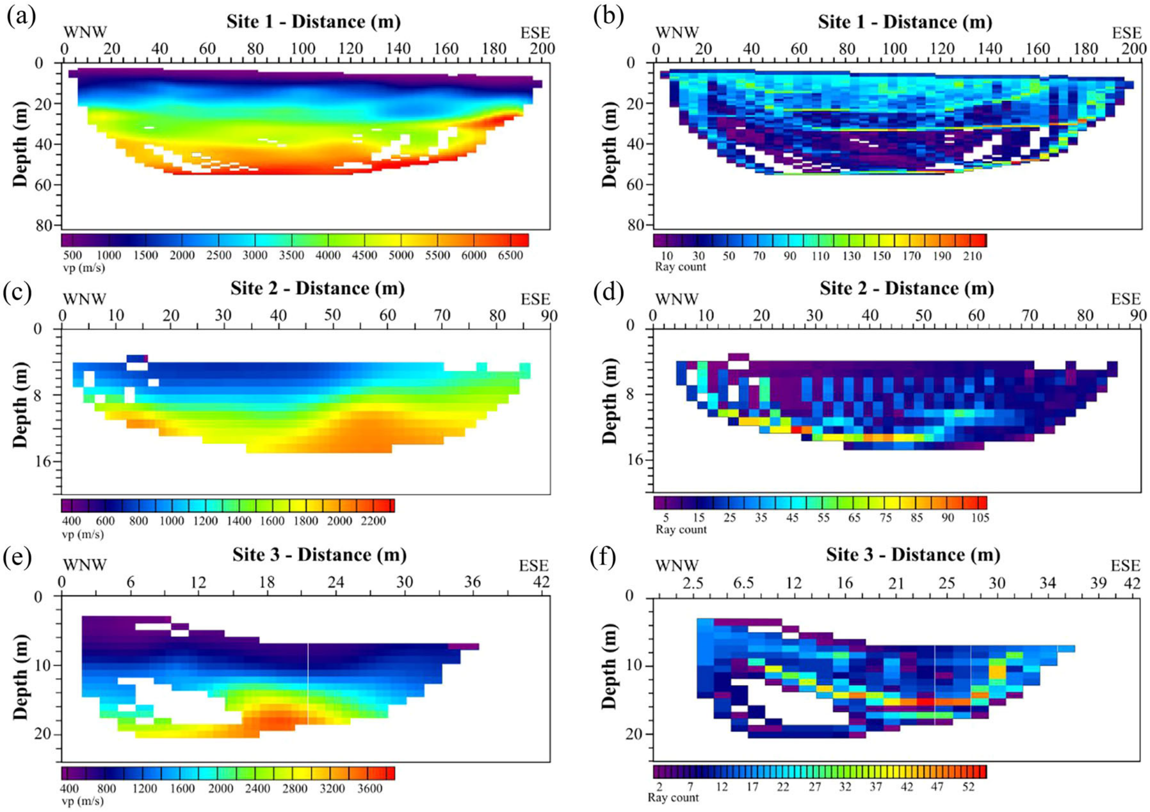

FIGURE 4 Overview of the P-wave first-break tomography models and their corresponding ray paths at Site 1 (a and b), Site 2 (c and d) and Site 3 (e and f), respectively.

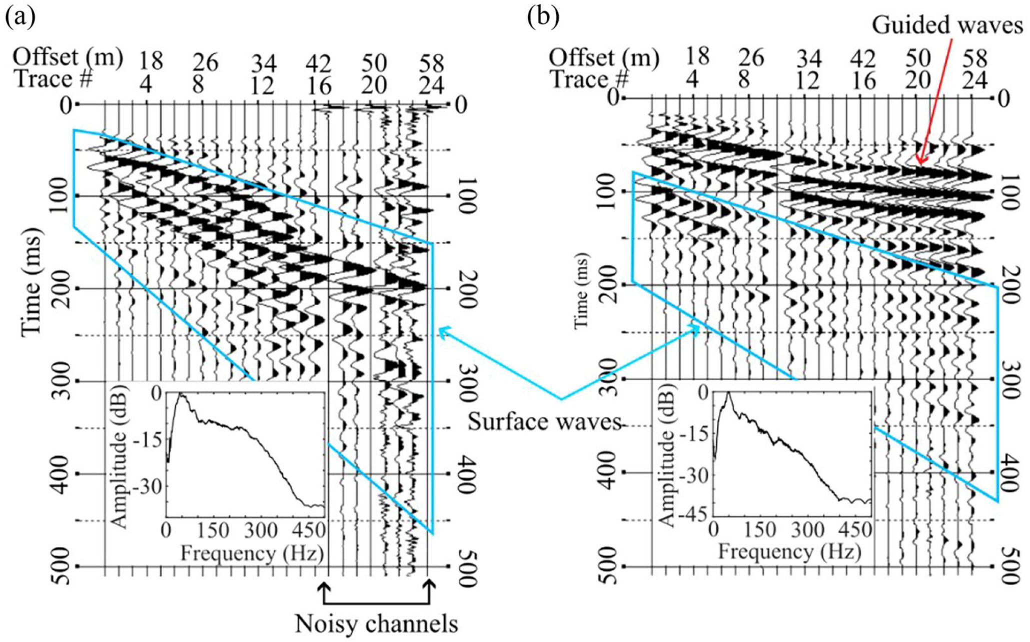

FIGURE 5 Typical quality shot gathers (with their corresponding amplitude spectra) from data collected at Site 3 (a) and Site 2 (b), respectively. The shot gathers highlight the presence of visible surface wave trends (blue polygons) along with guided waves (red arrow) and high frequency noise (marked using black double headed arrow).

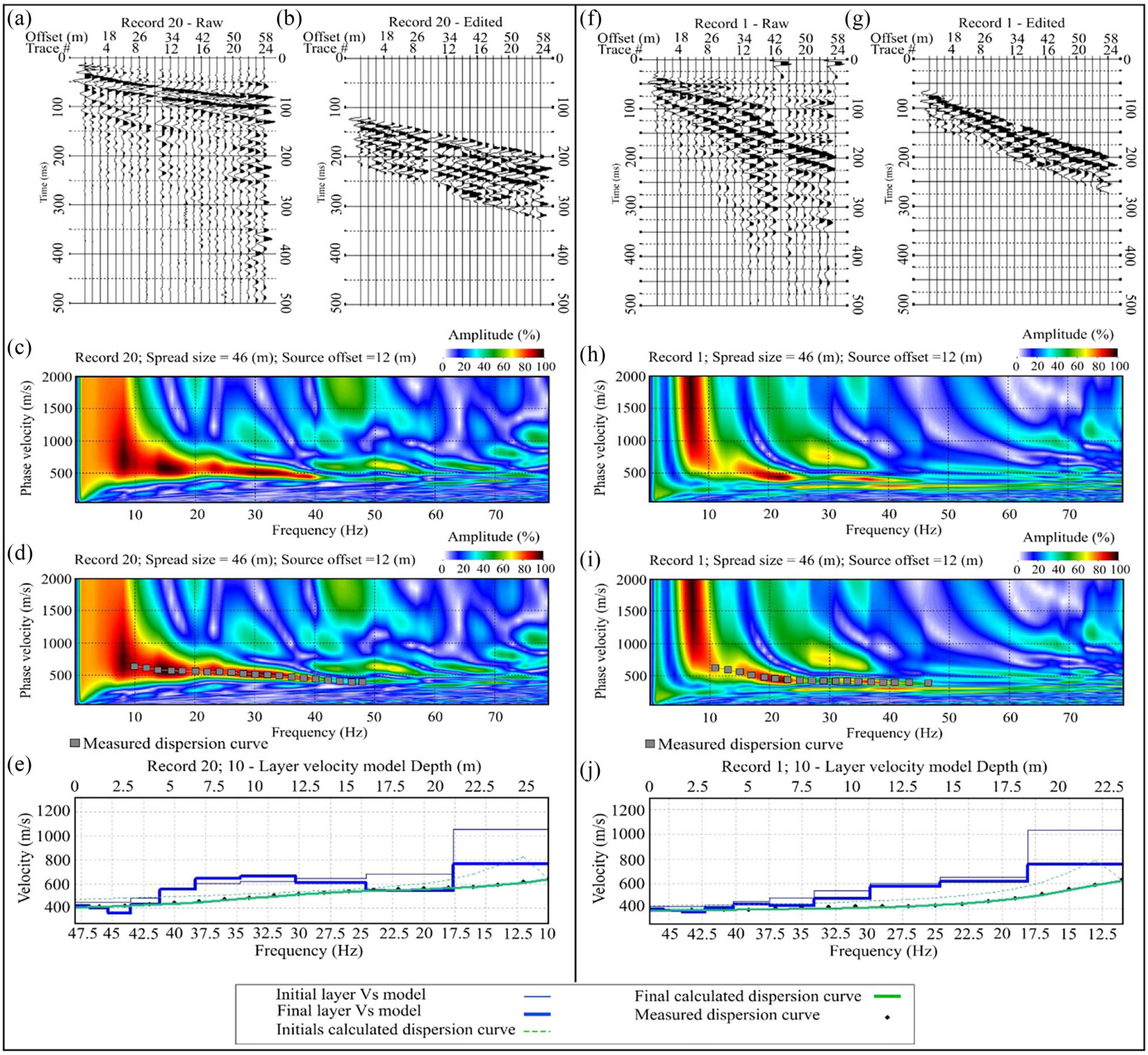

FIGURE 6 Surface wave processing workflow example from data gathered at Site 1 (a)–(e) and Site 3 (f)–(j). (a) Raw shot gather from Site 1. (b) Processed (muted) shot gather in (a). (c) Phase velocity-frequency spectra (dispersion image) of the processed shot gather in (b) obtained via the phase-shift transform method. The illustrated phase velocity-frequency spectra display the fundamental mode. (d) Phase velocity-frequency spectra illustrating the superimposed picks (dispersion curve) of the fundamental mode. (e) Final V_s profile model deduced from the dispersion curve in (d). Parts (f)–(j) are the raw shot gather, processed shot gather, phase velocity-frequency spectra, dispersion curve and final V_S profile model for record 1 data collected at Site 3, respectively.

length of 160 m and an electrode spacing of 4 m were used. At Sites 2 and 3, high-resolution profiles were acquired using a spread length of 80 m and an electrode spacing of 2 m. The takeout cables were connected to stainless steel electrodes hammered firmly into the ground. Rubber band ties were used to couple the take-out cables to the electrodes. The length of the acquired resistivity profiles was restricted by mining activities. A tape measure was used to deploy the electrodes along the measurement lines, for positional control, and a DGPS was used to record the location information of the survey lines. The data were acquired using an input current of 10 mA and a contact resistance with an upper threshold of 3000 ohms. As the top layer in the study area was dry and compacted in portions prior to data acquisition, all the electrodes were tested for contact resistance and erroneous readings. In areas of high contact resistance, the electrodes were hammered deeper and water mixed with a conducting solution was used to decrease the contact resistance, improve the conductivity of the rock material around the electrode and improve the electrode coupling. During the acquisition phase, the recorded measurements were monitored throughout. Table 1 gives the parameters and array types that were used to acquire the resistivity data at all sites.

The ERT data processing consisted of four steps, that is: (1) assessing and removing negative- and zero-voltage values; (2) system error assessment; (3) initial inversion and post-inversion error assessment; and (4) final inverse model computation. In resistivity surveys, negative- and zero-voltages can result due to induced polarization, geometrical arrangement of electrodes, 3D current effects caused by the presence of unconformities, poor electrode contact and damaged cables to mention a few (Glaser et al., 2021; Guo, 2015; Pain et al., 2002). The system error/measurement error assessment was evaluated using the stacking error, which is the coefficient of variation value supplied by ERT devices. The apparent resistivity data had a stacking error deviation of less than 0.1% (Figure 3c); thus, no data points were removed due to a high system error. After adequate quality assessment, the apparent resistivity data were inverted to obtain a true resistivity model of the near-surface. The inverse models were created using a triangular finite element mesh, which permits application to more complex geometry (Binley & Kemna, 2005; Blanchy et al., 2020). Inversion assessment was conducted after the calculation of the initial inverse model, and the data were filtered based on the inversion error. Data points with a normalized inversion error of <-3 and >3 were removed, and the inversion was recomputed to obtain a more accurate true resistivity model. An example of input data before and after normalized error filtering for P1 is illustrated in Figure 3d,e, respectively. Only two data points were removed from P1, and no points were removed from the P2 and P4 final inverse model computation as all data points fell within the acceptable normalized error range.

Data processing and inversion were computed in ResIPy, an open-source software that inverts data based on a regularized objective function combined with weighted least squares (Blanchy et al., 2020). All the calculated resistivity inverse models reached the target root square mean error of ~1 in three iterations.

RESULTS AND INTERPRETATIONS

The results of SRT, MASW and ERT data (Figures 7–9) were interpreted to understand the near-surface weathered zone, its secondary features (e.g. fractures) and interactions between surface water and groundwater. At all sites, SRT, MASW and ERT show a complex and variable near-surface. However, the P- and S-wave velocity and resistivity models are largely consistent.

Site 1

Figure 7 shows tomography-obtained P-wave (V_p) and MASW-obtained S-wave (V_S) velocities, their interpreted conceptual models and electrical resistivity results from Site 1. Both P-wave tomography and S-wave velocities illustrate a correlating increase in P- and S-wave velocity patterns with depth (Figure 7a–c). Additionally, the tomograms reveal the presence of three main layers, as depicted in the P- and S-wave conceptual models of the site (Figure 7d,e). The three main layers identified correspond to (1) overburden, (2) semi-weathered bedrock zone, and (3) least-weathered (fresh to minimally weathered crystalline) bedrock zones. The zones are characterized by P- and S-wave velocities ranging between: (1) <500–1500 and <400–700 m/s for the overburden; (2) 1500–3500 and 700–1400 m/s for the semi-weathered bedrock zone; and (3) >4000 and >1400 m/s for the least-weathered bedrock zones, respectively. The blue and white dashed lines in the conceptual models (Figure 7d,e) illustrate the depth and lateral variation in the P- and S-wave velocity layers with respect to the three identified zones and each other. Although the P- and S-wave results are similar both in depth and laterally, additional information is gained from the S-wave tomogram (Figure 7c). This discrepancy is likely due to the inherent smoothness of the P-wave first arrival ray-tracing tomography, where the velocities obtained are a factor of both the smoothness constraints and an average of different ray paths traversing the individual grid cells (i.e., Tryggvason et al., 2002), whereas no smoothness is introduced in the MASW inversion process. The MASW-obtained S-wave velocities are also able to resolve low-velocity zones underlying high-velocity zones, unlike the refraction P-wave results, which overall depict an increase in velocity with depth (compare Figure 7b,c).

The identified transitions between the overburden and semi-weathered bedrock zones are apparent in the ERT data (Schlumberger array, Figure 7f), and both zones are characterized by very low resistivities (<400 Ω m; dark blue to red colour zones). The black dashed line in Figure 7f,g is the depth to investigation (DOI) estimate. The DOI is a depth after which the anomalies observed in an inverse model are no longer constrained by the data and should not be interpreted geologically (Oldenburg & Li, 1999). A transparent sensitivity map is overlain from the depth of the DOI estimate to illustrate the low ERT sensitivity in the region. Figure 7f,g illustrates a very low resistivity distribution across the surveyed near-surface zone, varying from ~13 to 400 Ω m. The ERT section illustrates a positive correlation with the S-wave section (compare Figure 7g,h). Overall, both illustrate increasing resistivity and S-wave velocities with depth, increasing overburden thickness moving towards the northern side of the profile and higher resistivity

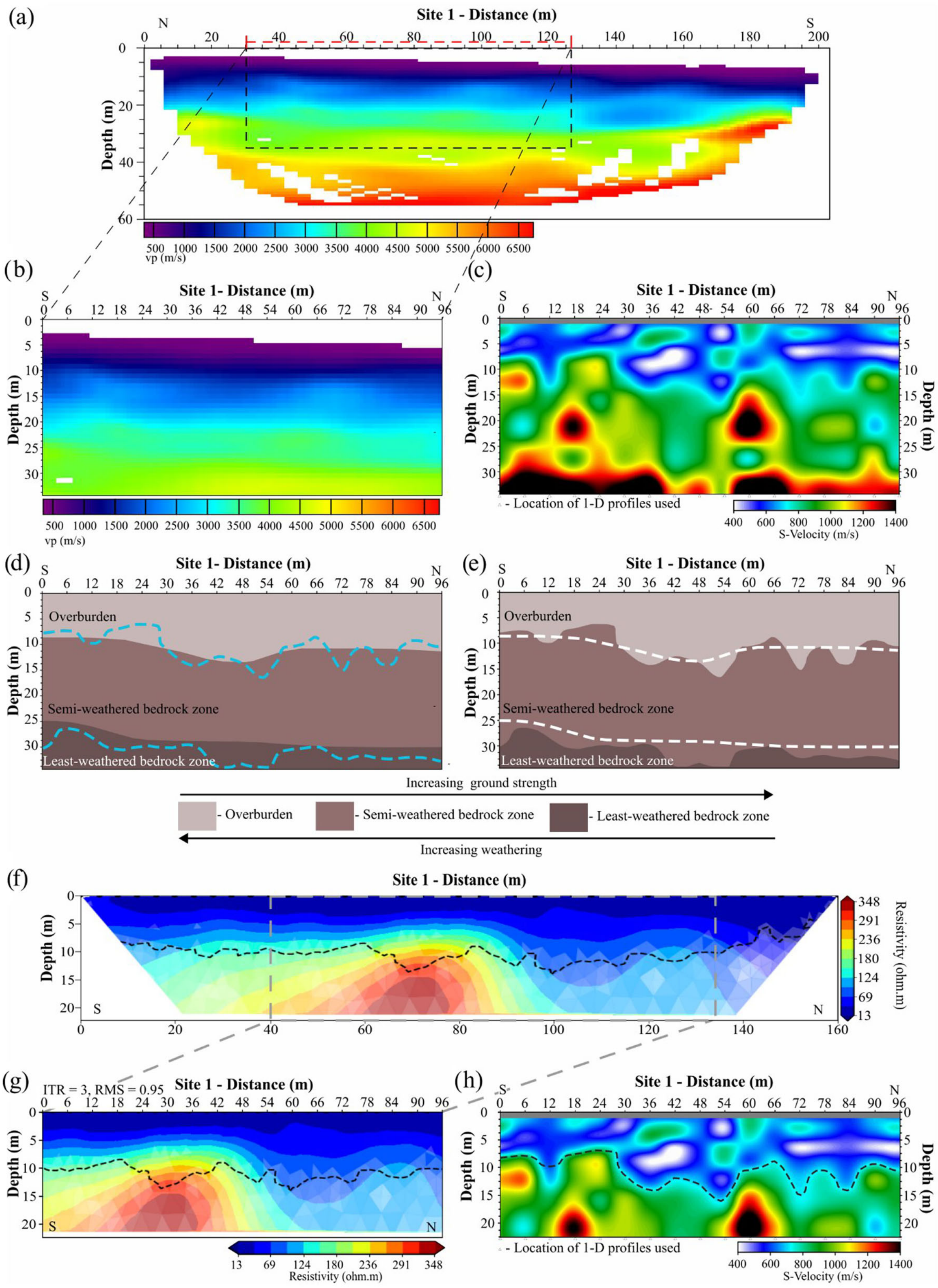

FIGURE 7 (a) P-wave first-break travel-time tomography obtained at Site 1. (b) P-wave first-break travel-time tomography along the multichannel analysis of surface waves (MASW) profile location. The red dashed line between lateral distances 30 and 126 m, in (a), shows the P-wave profile location corresponding with the MASW profile location. (c) Tomographic pseudo-2D S-wave model derived from the analysis of surface waves at Site 1. Parts (d) and (e) are interpreted conceptual models for the P-wave tomography and S-wave velocities in (b) and (c), respectively. The conceptual models show the variation in weathering with depth. The dashed blue lines in (d) show the interpreted overburden/semi-weathered and semi-weathered/least-weathered boundaries deduced from the tomographic pseudo-2D S-wave model in (c) and projected onto the P-wave tomography conceptual model, whereas the dashed white line in (e) the P-wave tomography projected onto the tomographic S-wave conceptual model. (f) Electrical resistivity (Schlumberger array) results along the presented P-wave and S-wave location at

(Continues)

FIGURE 7 (Continued)
Site 1. (g) Cropped electrical resistivity section correlating with the presented Site 1 P-wave and S-wave sections. The black dashed line in (f) and (g) is the depth to investigation (DOI) estimate. (h) Cropped Site 1 S-wave velocity section corresponding with (g).

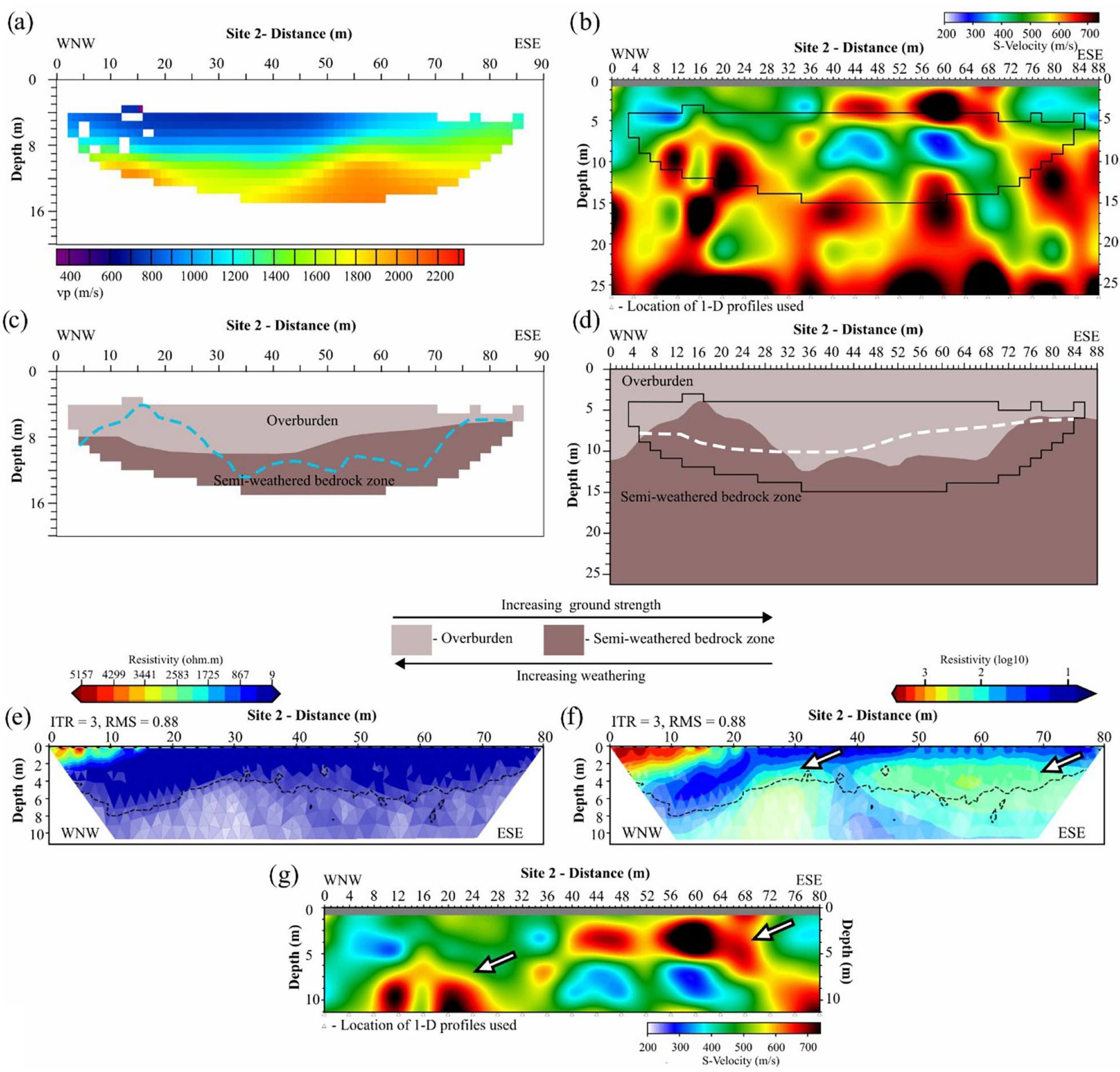

FIGURE 8 (a) P-wave first-break travel-time tomography for Site 2. (b) Tomographic pseudo-2D S-wave model derived from the analysis of surface waves obtained at Site 2. Parts (c) and (d) are conceptual models for the P-wave tomography and S-wave velocities in (a) and (b), respectively. The interpreted conceptual models show the variation in weathering with depth. The dashed blue line in (c) illustrates the interpreted overburden/semi-weathered boundary deduced from the S-wave velocities in (b) and projected onto the P-wave tomography conceptual model, whereas the dashed white line in (d) the P-wave tomography projected onto the S-wave tomography. (e) Electrical resistivity (Schlumberger array) pseudosection and (f) is the peudosection in (e) projection in log form. The black dashed line in (f) and (g) is the depth to investigation (DOI) estimate. (g) Cropped Site 2 S-wave velocities corresponding with (e and f). The white arrows indicate correlating regions of the electrical resistivity tomography (ERT) and S-wave pseudosections.

and S-wave velocities on the southern side of the profile. Considering that this area consists of crystalline rocks (i.e., norites and melanorites), which have negligible intergranular porosity, the low resistivities are most likely due to high conductivity along cracks and fissures, and the presence of charged particles associated with weathering of the crystalline rocks. Unfortunately, the resistivity section appears to rapidly lose sensitivity with depth, rendering the profile rather smooth at depth.

Overall, the general variation of the overburden/semi-weathered bedrock transition zone in the ERT, P- and S- wave sections at this site is correlated moving from

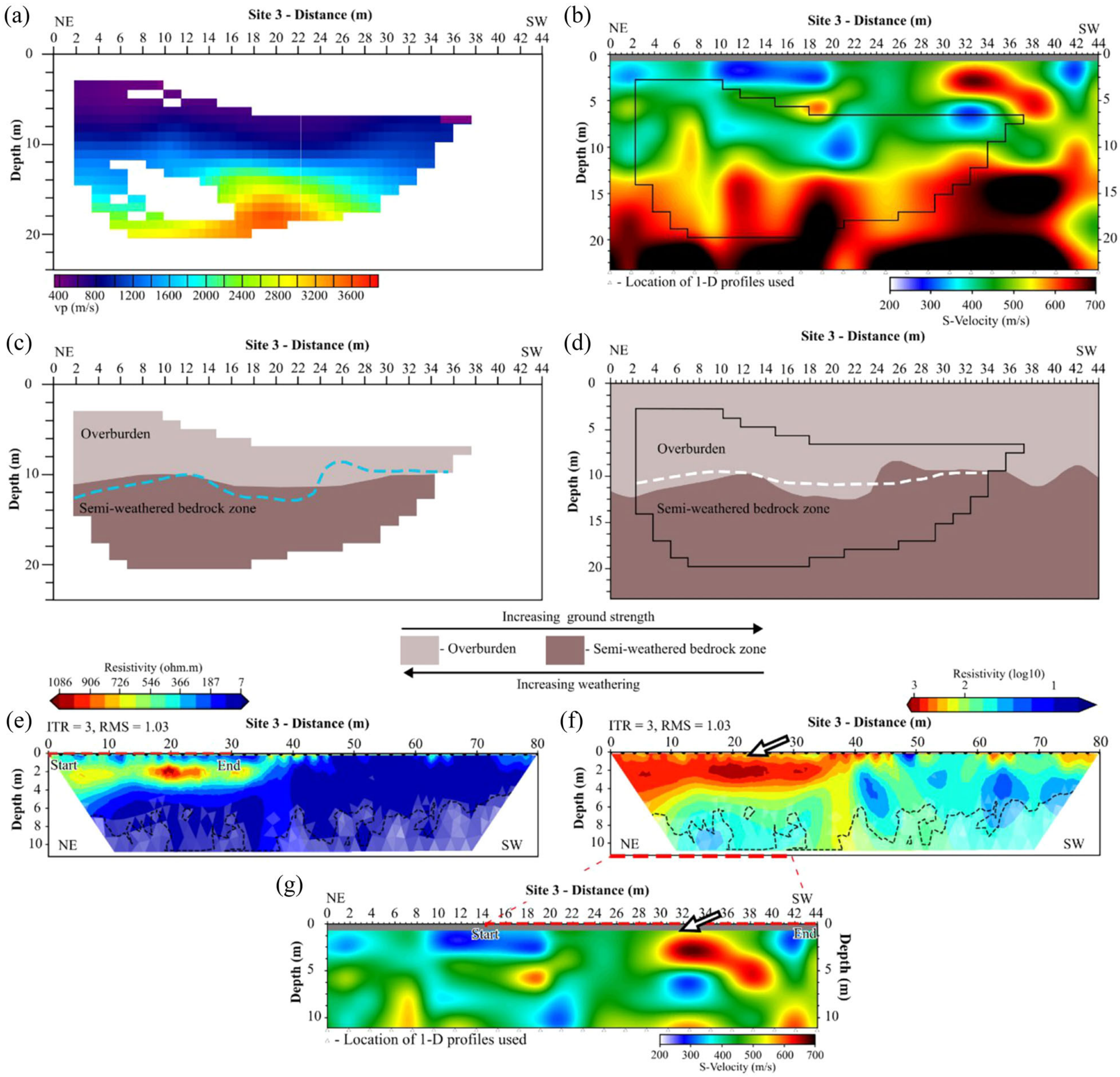

FIGURE 9 (a) P-wave first-break travel-time tomography obtained at Site 3. (b) Tomographic pseudo-2D S-wave model derived from the analysis of surface waves obtained at Site 3. Parts (c) and (d) are interpreted conceptual models for the P-wave tomography and S-wave velocities in (a) and (b), respectively. The conceptual models show the variation in weathering with depth. The dashed blue line in (c) illustrates the interpreted overburden/semi-weathered boundaries deduced from the tomographic pseudo-2D S-wave model in (b) and projected onto the P-wave tomographic conceptual model, whereas the dashed white line in (d) the P-wave tomography projected onto the tomographic S-wave conceptual model. (e) Electrical resistivity (Schlumberger array) pseudosection and (f) is the peudosection in (e) projection in logarithmic scale. The black dashed line in (e) and (f) is the depth to investigation (DOI) estimate. (g) Cropped Site 3 S-wave velocity section corresponding with (e and f). The red dashed lines in (e)–(g) illustrate where the profiles overlap. Start indicates the overlap starting point and End indicates the overlap end point. The white arrows indicate correlating regions of the electrical resistivity tomography (ERT) and S-wave pseudosections.

the south to the north side of the profiles. The obtained resistivities, P- and S-wave velocities, for the top 20 m mapped by all methods, are generally low, ranging between ∼<13 and ∼350 Ω m in the resistivity section, ∼<500 and ∼3500 m/s in the P-wave section, and ∼400 and ∼1000 m/s in the S-wave section. Considering that fresh rocks often have resistivities of around 2000–3000 Ω m, P-wave velocities >3000 m/s and shear-wave velocities greater than >1500 m/s, therefore implies the presence of possible water saturation, conductive and less compact sediments (Gomo et al., 2023; Kirsch, 2006).

Site 2

Figure 8 shows the P- and S-wave velocity sections obtained at Site 2, along with their corresponding conceptual models, and the resistivity results. Here, the P- and S-wave tomograms vary when compared to one another (compare Figure 8a,b), which is most likely due to the presence of low S-wave velocity zones (green-blue zones) below high-velocity zones (yellow-red-black zones) in the near-surface region (Figure 8b). The P-wave velocities range between <400 and ∼2300 m/s, whereas the S-wave velocities range between 200 and ∼700 m/s. Both P- and S-wave velocity ranges are quite low, indicating deep weathering, with only the overburden and semi-weathered bedrock zones resolved (Figure 8c,d).

Figure 8e,f shows the electrical resistivity (Schlumberger array) at the site in linear and logarithmic form, respectively, whereas Figure 8g illustrates a cropped S-wave velocity section, corresponding with the resistivity sections in Figure 8e,f. The black dashed line in Figure 8e,f illustrates the DOI estimate. Figure 8e illustrates a very low resistivity distribution across the surveyed near-surface zone. A direct correlation is observed between the electrical resistivity and S-wave sections as compared to the P- and S-wave velocity sections (compare Figure 8f,g). Similar to results obtained at Site 1, the resistivity and S-wave velocities of the shallow-seated rocks at Site 2 are overall low, largely ranging between ∼7 and 570 Ω m, and ∼200 and 700 m/s, respectively. Within the mapped near-surface zone (i.e., the top ∼12 m), there are three zones of higher resistivity (observed as light green-, yellow-, red- and black-coloured zones). The first zone, characterized by the highest resistivity (∼700–4946 Ω m), is located on the western side of the profile, situated at a lateral distance of 0 to ∼16 m and extending from the surface to a depth of ∼3 m. This zone is interpreted to correspond to a zone of boulders (see Gomo et al., 2023). The second resistivity high zone (∼60–600 Ω m) is situated at a lateral distance of ∼10 to ∼35 m and extends from a depth of ∼3 to ∼12 m. The third resistivity high zone, with similar resistivities to the second high resistivity zone, is observed on the western side of the profile, at a lateral distance between 35 and 80 m, and at a depth between ∼2 and 12 m. Both second and third resistivity high zones are overlain by and enclose a low resistivity zone (∼12–70 Ω m), which extends to depths beyond the ERT survey limits. Both the second and third resistivity high zones and the resistivity low zone present on the ERT section are closely matched by the S-wave results (compare Figure 8f,g). The high resistivity and high-velocity S-wave zones likely correspond to least-weathered and least-water- and salt-saturated zones. The low resistivity and shear-wave velocity zones (dark-light blue to greenish coloured zones) separating the resistivity high zones are interpreted as a highly weathered zone with a possible high content of conductive minerals and/or water- and salt-saturation, which is altogether a zone that is likely highly hydraulically conductive.

Site 3

Figure 9 shows P- and S-wave tomograms at Site 3, along with their corresponding conceptual models, and resistivity results obtained at the site. Similar to the P- and S-wave sections at previous sites, the tomograms at this site reveal the presence of two zones, that is the overburden and semi-weathered bedrock. The overburden is characterized by P-wave velocities ranging from ∼400 to 1500 m/s and S-wave velocities ranging from 200 to ∼650 m/s. The semi-weathered bedrock layer is characterized by P-wave velocities ranging from ∼1500 to 3800 m/s and S-waves ranging between ∼650 and 700 m/s. The P- and S-wave results are well correlated with each other (compare Figure 9a,b), and, similar to the other sites, S-wave results demonstrate the presence of least-weathered zones within the overburden zone and highly-weathered zones, both within the semi-weathered near-surface zone.

Figure 9e,f shows the electrical resistivity pseudosection (Schlumberger arrays) at the site in linear and logarithmic form, respectively. The black dashed line in Figure 9e,f is the DOI estimate. Figure 9g illustrates a cropped S-wave velocity results, generated from Figure 9b at Site 3, largely corresponding with the resistivity sections in Figure 9e,f. Notably, the first lateral 30 m of the resistivity section corresponds with the last 30 m of the S-wave section, indicated by red dashed lines on the figure. At the depths resolved by the resistivity survey (from 0 to ∼11 m below surface), obtained resistivities and S-wave velocities are generally low, similar to those at the two previous sites investigated, ranging between ∼3 and ∼1200 Ω m, and ∼200 and ∼700 m/s, respectively. Like at other sites, these results also suggest extensive weathering, and the presence of conductive and less compact near-surface sediments. Within the mapped low-resistivity and S-wave velocity zones, on the northeastern flank, from a depth of ∼2 to 7 m and at lateral distances between 0 and ∼45 m on the resistivity section (Figure 9e,f); and from a lateral distance of 18 to 42 m on the S-wave section (Figure 9g), notable near-surface high resistivity (>400 Ω m, dark red-black coloured) and S-wave velocity (yellow-red coloured) zones (>500 m/s) are observed. These zones are interpreted as least-weathered dense soils, possibly also containing boulders. The high resistivity and S-wave velocity features also exhibit discontinuities, or lower resistivity and S-wave zones (high hydraulic conductivity zones), which are likely caused by rock mass fracturing. At depths around 12 m, the low shear-wave velocity zone is underlain by a zone of higher shear-wave

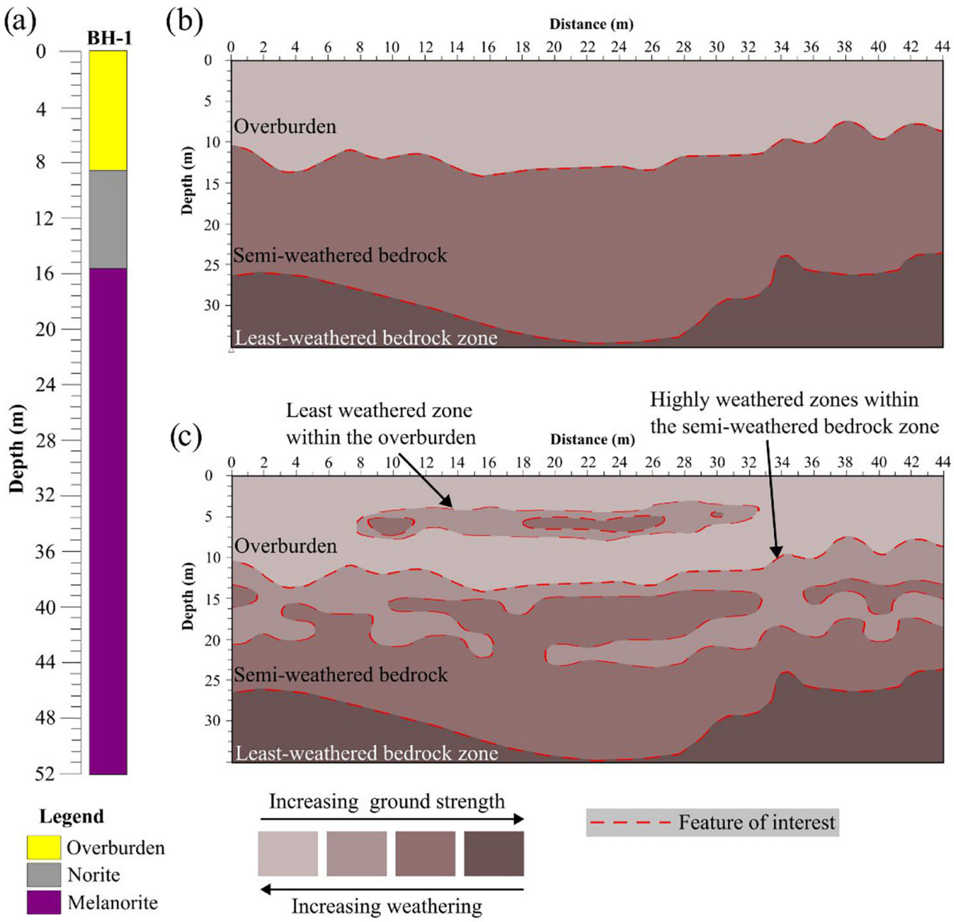

FIGURE 10 (a) Borehole BH-1, taken from approximately 1.5 km west of the study sites. The borehole illustrates the rock types present in the study area. (b) Conceptual model of the study area, deduced from the knowledge obtained from the acquired data, illustrating variation in layering/ground strength/weathering. (c) Complex weathering within the overburden and semi-weathered zones. No weathering detail is given for the least-weathered bedrock zone to avoid over-interpretation.

velocity (>600 m/s), better observed in Figure 9b, likely corresponding to the semi-weathered bedrock zone.

DISCUSSION AND INTERPRETATION

The P-wave, S-wave and electrical resistivity tomograms provide a basis for the interpretation of near-surface characteristics in the study area. In Figure 10, we propose an interpretative geological cross-section of the near-surface aquifer zone at the mine, based on borehole data combined with all geophysical methods applied at the three sites.

Overburden characteristics

The overburden, which constitutes the top ~9 m of the study area, is characterized by low resistivities, and low P- and S-wave velocities (Figures 7–9). These results indicate a high electrical conductivity and high weathering within the overburden, in turn suggesting a high porosity and clay content zone (which can be very conductive in a wet medium), with moderate-to-high levels of moisture held by soil particles and a possible high availability of nutrients/soluble salts (e.g., sodium, calcium, magnesium and potassium) (Grisso et al., 2005; Theron & van Niekerk, 1934). Results from this study align with the overburden characteristics of the area (Figure 10a). Specifically, Theron and van Niekerk (1934) detailed that the region is characterized by black turf soil (heavy clay soil) that is highly fertile (nutrient-rich) and capable of retaining moisture. The soil formed from the chemical weathering of the underlying RLS rocks (i.e., norite and melanorite in the study area). Black turf soil is readily pervious to water (permeable) but has a high water-holding capacity that reduces leaching, especially in sub-humid and semi-arid climatic zones. The soil has a highly developed crumb structure and a clay content that varies from 40% to 60%, and a moisture equivalent commonly ranging between 40% and 50% (Oppermann et al., 2017; Theron & van Niekerk, 1934). The turf soil overburden in the western Bushveld Complex varies between ~1 and 5 m in thickness (De Klerk, 1982; Oppermann et al.,

TABLE 2 Surface wave seismic velocity and electrical resistivity physical property table of rocks (modified after Kirsch, 2006).

Soil profiles type	Rock/soil description	Average S-wave velocity (m/s) top 30 m	Rock type	Resistivity (Ω m)
A	Hard rock	>1500	Gravel, sand (dry)	500–2000
B	Rock	760–1500	Gravel, sand (saturated)	40–200
C	Very dense soil/soft rock	360–760	Fractured rock	60–2000
D	Stiff soil	180–360	Solid rock	>2000
E	Soft soil	<180	Till	30–60
F	Special soils requiring site-specific evaluation	–	Clay	10–30

2017). Within the overburden, black turf soils constitute the A-horizon. The A-horizon progresses into the yellow-coloured C-horizon, which varies greatly in depth (from 12 to 50 m) and consists of partially weathered mafic rocks (Titus et al., 2009). The C-horizon is underlain by the R-horizon, which corresponds to unweathered bedrock, characterized by norite and melanorite in the studied area (Figure 10a). Together, the A–AC–C horizons constitute the soil horizon sequence of the study area (Oppermann et al., 2017; Theron & van Niekerk, 1934).

Near-surface setting and water inflow implications

The low P- and S-waves velocities, and resistivity zone at the sites of interest (Figure 2), largely extend from the surface to depths greater than those resolved by the P-wave (excluding at Site 1), S-wave and electrical resistivity surveys (Figures 7–9). The overburden zone, characterized as a low P-wave, S-wave and electrical resistivity zone, suggests highly to semi-weathered and possibly fractured rocks (Table 2). According to available borehole data, located approximately 1.5 km west of the study areas, the stratigraphic sequence (up to 54 m) begins with the overburden, characterized as a highly weathered soil to saprolite zone, extending to a depth of ~9 m. With increasing depth, the overburden is underlain by norite (~9 m) and finally melanorite (>36 m) (Figure 10a). We observe a good correlation when comparing the thickness of the identified overburden zone from the P-wave, S-wave and resistivity sections with the borehole data (compare Figures 7–9). Unfortunately, due to the dipping nature of the RLS rocks and the distance of the borehole from the studied sites, the variation of P-waves, S-waves and electrical resistivity sections at depths greater than the overburden zone could not be determined. Overall, results suggest that in the studied sites, the variation in the weathered zone (i.e., from overburden to semi-weathered bedrock in Figure 10b,c) is complex and extends to a depth greater than that suggested by the borehole data (compare depths from Figure 10a,b). This is not surprising, as the western portion of the Bushveld Complex is characterized by deep weathering, extending approximately 25–40 m deep (Hey, 1999; Junge et al., 2019).

In the inversion models, roughly where norite appears in the borehole data (i.e., about 9 m deep), the P- and S-wave velocities and electrical resistivities (at Site 1) increase altogether, suggesting a boundary and presence of a semi-weathered bedrock zone (norite/melanorite) below the overburden zone. This zone is better observed in both the P- and S-waves sections (Figures 7–9). The semi-weathered bedrock zone appears to be highly fractured and possibly water- and salt-saturated (Table 2; Kirsch, 2006). In the western portion of the Bushveld Complex, Gebrekristos and Cheshire (2012) reported that the depth of the semi-weathered (weathered aquifer) zone extends to approximately 35 m, similar to the maximum depth of the semi-weathered bedrock zone mapped at the Tharisa Minerals (Figures 7). Furthermore, Gebrekristos and Cheshire (2012) stated that the depth and degree of weathering (including in this zone) varies across the Bushveld Complex and is dependent on the underlying lithologies and site-specific physio-chemical conditions. Considering that pre-mining studies conducted within the Tharisa Minerals region established that groundwater levels were, on average, 10 m below ground level (mbgl) and had a depth range of 2–30 mbgl (Cuthbertson, 2022), it is likely that the overburden zone forms part of the weathered aquifer zone, which is characteristic of the Bushveld Complex.

Below the semi-weathered bedrock aquifer zone is the least-weathered (crystalline) bedrock zone (Figure 7). The results demonstrate a clear succession from overburden (soil-boulder zone) to semi-weathered bedrock zone (corresponding to the weathered aquifer zone), to the least-weathered (crystalline) bedrock zone with increasing depth, as depicted in the conceptual model of the study area (Figure 10b,c). It is likely that the least-weathered bedrock zone is fractured and weathered to depths beyond those mapped by the surveys, as indicated by published reports (Fourie et al., 2017; Govender, 2019; Hey, 1999; Junge et al., 2019; Lourens, 2013; Van Wyk, 2013). Generally, in the absence of secondary fractures, the least-weathered bedrock zone forms poor aquifers (in fact, aquitards) due to the insignificant porosity of the rocks. In the presence of regional and/or secondary fractures, high-yielding aquifers can develop in this crystalline rock zone. The aquifer (i.e., the crystalline aquifer) formed in the least-weathered bedrock zone is often connected with the weathered aquifers and can extend to depths of about 130–140 m below ground level (Gebrekristos & Cheshire, 2012).

Our results suggest that, within the near-surface, water inflow into the pits at Tharisa Minerals is, therefore, most probably sourced from both the weathered and least-weathered (crystalline) aquifers, as mining is currently happening at depths (currently 120 m) below and within the water level of these aquifers (i.e., at 120 mbgl). In addition to the weathered and least-weathered aquifers, there lies a possibility that more sources contribute to the flow of water inside the mine, such as the river (Sterkstroom River) cross-cutting the mine lease area, alluvial aquifers associated with the river, non-perennial rivers and streams in the area, a dyke cross-cutting the Sterkstroom River and Tharisa Minerals pits, and other geological structures present in the vicinity of the mine, making it a possible combined effect of both near-surface groundwater and the surface water flow systems.

Water inflow reduction recommendations

A hydrogeological-geophysical study conducted by Dildar et al. (2023) at Tharisa Minerals illustrated that the water flooding the opencast pits is coming from multiple sources: surface water, shallow bedrock aquifer/s and from deep sources (from which water seeps into the pit, from beneath the pit floor, via lineaments prevalent in the crystalline rock zone and those caused by mining activity). Thus, to reduce the water inflow as mining progresses to greater depths, a combination of dewatering techniques could be implemented considering the multiple sources found in the vicinity of the mine and their depth ranges. Dewatering techniques mainly assist with dropping the potentiometric surface in the vicinity of the mine, which improves pit working conditions, safety, pollution water control, production and associated mining costs (Preene, 2015; Straskraba, 2014).

CONCLUSION

We used an integrated geophysical approach involving SRT, MASW and ERT methods to map and characterize weathered bedrock aquifer systems at Tharisa Minerals (Bushveld Complex). The surveys produced complex but largely correlating and complementary geophysical results. All three methods mapped zones of increasing velocities and resistivities quite well, whereas the MASW and ERT methods mapped low-velocity and resistivity zones within the near-surface in a satisfactory and complementary manner, demonstrating the advantages of conducting integrated studies.

Generally, the results reveal the prevalence of extensive and deep weathering, possible high hydraulic conductivity zones and variable weathering with depth. Variation of the aforesaid is mainly associated with the overburden zone, semi-weathered bedrock zone (which hosts the weathered aquifer) and the crystalline bedrock zone, where aquifers are associated with joints and fractures. Currently, the pit at Tharisa Minerals is about 120 m deep; consequently, mining activities occur in both the weathered and crystalline aquifer zones. Water inflows are produced by the flow of water from surface, weathered and crystalline aquifers. To mitigate uncontrollable block flooding, possibly improving pit working conditions and increasing production, dewatering techniques targeting to improve water inflow control inside the pits should be considered.

ACKNOWLEDGEMENTS

We would like to acknowledge Tharisa Minerals (South Africa) for funding this project and giving us permission to publish this work. Special thanks are due to the NRF (National Research Foundation), Wits Seismic Research Centre and DSI-NRF CIMERA (Centre of Excellence for Integrated Mineral and Energy Resource Analysis) for funding this research project. We also wish to extend our gratitude to the postgraduate students from the School of Geosciences at the University of the Witwatersrand who assisted with the data collection and Tharisa Minerals staff, especially Hloniphani Hlongwa and Robey Labuschagne, for assisting us during the data acquisition. Special thanks to Nathi Mntungwa from Tharisa Minerals for scientific discussions and support. The authors also thank two anonymous reviewers for their comments which have greatly improved this study. Finally, Dr. Mark Vardy is thanked for editorial handling.

CONFLICT OF INTEREST STATEMENT

The author declares no conflicts of interest.

DATA AVAILABILITY STATEMENT

The data that support the finding of this study are available from Tharisa Minerals. Restrictions apply to the availability of these data, which were used under the license for this study. Data are available from author with the permission of Tharisa Minerals.

ORCID

Sikelela Gomo https://orcid.org/0000-0002-3098-0308
Musa S.D.Manzi https://orcid.org/0000-0002-1654-5211
Bojan Brodic https://orcid.org/0000-0003-4694-9847

Ian James https://orcid.org/0000-0002-1655-3529
Gordon R.J. Cooper https://orcid.org/0000-0003-2864-2542

REFERENCES

Akintoriwa, O.J. & Olowolafe, T.S. (2013) Geoelectric evaluation of groundwater prospect within Zion Estate, Akure, Southwest, Nigeria. *International Journal of Water Resources and Environmental Engineering*, 5, 12–28. Available from: https://doi.org/10.5897/IJWREE12.031

Alcala, F.J., Martinez-Pagan, P., Navarro, M., Perez-Cuevas, J. & Domingo, F. (2021) Combining of MASW and GPR imaging and hydrogeological survey for the groundwater resource evaluation in a coastal urban area in southern Spain. *Applied Science*, 11, 3154. Available from: https://doi.org/10.3390/app11073154

Ali, A., Ullah, M., Barkat, A., Raza, W.A., Qadir, A. & Qamar, Z. (2021) Multi-channel analysis of surface waves (MASW) using dispersion and iterative techniques: implications for cavity detection and geotechnical site investigation. *Bulletin of Engineering Geology and the Environment*, 80, 9217–9235. Available from: https://doi.org/10.1007/s10064-021-02485-y

Al-Heety, A.J.R., Hassouneh, M.M. & Abdullah, F.M. (2021) Application of MASW and ERT methods for geotechnical site characterization: a case study for roads construction and infrastructure assessment in Abu Dhabi. *UAE. Journal of Applied Geophysics*, 193, 104408. Available from: https://doi.org/10.1016/j.jappgeo.2021.104408

Binley, A. & Kemna, A. (2005) DC resistivity and induced polarization methods. In: Rubin, Y. & Hubbard, S.S. (Eds.) *Hydrogeophysics, water science and technology library*, vol. 50. Dordrecht: Springer, pp. 129–156. Available from: https://doi.org/10.1007/1-4020-3102-5_5

Blanchy, G., Saneiyan, S., Boyd, J., McLachlan, P. & Binley, A. (2020) ResIPy, an intuitive open-source software for complex geoelectrical inversion/modeling. *Computers and Geosciences*, 137, 104423.

Boorman, S., Boudreau, A. & Kruger, F.J. (2004) The Lower Zone-Critical Zone transition of the Bushveld Complex: a quantitative textural study. *Journal of Petrology*, 45, 1209–1235. Available from: https://doi.org/10.1093/petrology/egh011

Brodic, B., Malehmir, A., Pugin, A. & Maries, G. (2018) Three-component seismic land streamer study of an esker architecture through S- and surface wave imaging. *Geophysics*, 86, B339–B353. Available from: https://doi.org/10.1190/GEO2017-0747.1

Cawthorn, R.G. (2015) The Bushveld Complex, South Africa. In: Charlier, B., Namur, O., Latypov, R. & Tegner C. (Eds.) *Layered intrusions*. Singapore: Springer, pp. 517–587. Available from: https://doi.org/10.1007/978-94-017-9652-1_12

Cuthbertson, S. (2022) *Environmental management programme amendment application Tharisa Mine, North West Province*. Rivonia: GSC. Available from:

De Klerk, W.J. (1982) *The geology, geochemistry and silicate mineralogy of the Upper Critical Zone of the north-western Bushveld Complex, at Rustenburg Platinum Mines, Union section* [Unplublished M.Sc. Thesis]. Grahamstown: Rhodes University.

Dildar, J., Manzi, M.S.D., Abiye, T., Gomo, S., Rapetsoa, M.K. & Drennan, G. (2023) Groundwater circulation in the shallow crystalline aquifer of Tharisa Mine, South Africa: evidence from environmental isotopes and near-surface geophysics. *Water*, 15, 2876. Available from: https://doi.org/10.3390/w15162876

Eales, H.V. & Cawthorn, R.G. (1996) The Bushveld Complex. In: *Layered intrusions*. Amsterdam: Elsevier, pp. 181–229.

Fourie, F.D., Allwright, A.J., Makiwane, N. & Govender, N. (2017) Characterisation and protection of deep aquifers in South Africa: Characterisation [Extended abstract]. In *15th Biennial Ground water Conference*. London: International Association of Hydrogeologists. 1–14.

Gabriel, G., Kirsch, R., Siemon, B. & Wiederhold, H. (2003) Geophysical investigation of buried Pleistocene subglacial valleys in Northern Germany. *Journal of Applied Geophysics*, 53, 159–180. Available from: https://doi.org/10.1016/j.jappgeo.2003.08.005

Gebrekristos, R. & Cheshire P. (2012) Hydrogeological properties of the UG2 pyroxenite aquifers of the Bushveld Complex. [Extended abstracts] In *Proceedings of the 5th Platinum Conference of the Southern African institute of Mining and Metallurgy*, Southern Africa: The Southern African Institute of Mining and Metallurgy. pp. 143–152.

Glaser, D.R., Burch, K., Brinkley, D.L. & Reppert, P. (2021) Localization of deep voids through geophysical signatures of secondary dewatering features. *Geophysics*, 86(3), WA139–WA152.

Gomo, S., Rapetsoa, M.K., Manzi, M.S., Onyebueke, E., Dildar, J., Sihoyiya, M. et al. (2023) Integrated geophysical methods for boulder delineation to improve mining. *Geophysical Prospecting*, 71, 1–21. Available from: https://doi.org/10.1111/1365-2478.13322

Govender, N. (2019) *Characterisation of the deep aquifers of South Africa—the Bushveld Igneous Complex, crystalline basement rocks and dolomite formations* [Ph.D. Thesis]. Bloemfontein: University of the Free State, pp. 131.

Grisso, R.D., Alley, M.M., Holshouser, D.L. & Thomason, W.E. (2005) *Precision farming tools: soil electrical conductivity*. Blacksburg: Virginia Cooperative Extension.

Guo, K. (2015) *Towards 3D direct current resistivity and induced polarization imaging*. Toronto: University of Toronto.

Hasan, M., Shang, Y., Meng, H., Shao, P. & Yi, X. (2021) Application of electrical resistivity tomography (ERT) for rock mass quality evaluation. *Nature*, 11, 23683. Available from: https://doi.org/10.1038/s41598-021-03217-8

Hey, P.V. (1999) The effects of weathering on the UG2 chromitite reef of the Bushveld Complex, with special reference to the platinum-group minerals. *South African Journal of Geology*, 3, 251–260.

Roberts, M.K.C. & Clark-Mostert, V. (2010) Is there some commonality between the geological structures in the Bushveld Complex and the Great Dyke? In: The 4th international platinum conference, platinum in transition 'Boom or Bust'. Johannesburg: The Southern African Institute of Mining and Metallurgy. 118, pp 149–155.

Junge, M., Oberthur, T., Kraemer, D., Melcher, F., Pina, R., Derrey, I.T. et al. (2019) Distribution of platinum-group elements in pristine and near-surface oxidized Platreef ore and the variation along strike, northern Bushveld Complex, South Africa. *Mineralium Deposita*, 54, 885–912. Available from: https://doi.org/10.1007/s00126-018-0848-7.pdf

Junge, M., Oberthur, T., Osbahr, I. & Gutter, P. (2016) Platinum-group elements and minerals in the lower and middle group chromitites of the western Bushveld Complex South Africa. *Mineralium Deposita*, 51, 841–852. Available from: https://doi.org/10.1007/s00126-016-0676-6

Kirsch, R. (2006) *Groundwater geophysics—a tool for hydrogeology*. Singapore: Springer.

Lourens, P.J.H. (2013) The relation between South African geology and geohydrology. [M.Sc. thesis]. Bloemfontein: University of the Free State, pp. 164.

Malehmir, A., Bergman, B., Anderson, B., Sturk, R. & Johansson, M. (2018) Seismic imaging of dyke swarms within the Sorgenfrei-Tornquist Zone (Sweden) and implications for thermal energy storage. *Solid Earth*, 9, 1469–1485. Available from: https://doi.org/10.5194/se-9-1469-2018

Oldenburg, D.W. & Li, Y. (1999) Estimating depth of investigation in dc resistivity and IP surveys. *Geophysics*, 64(2), 403–416. Available from: https://doi.org/10.1190/1.1444545

Oppermann, L., Junge, M., Schuth, S., Holtz, F., Schwarz-Schampera, U. & Sauheitl, L. (2017) Mobility and distribution of palladium and platinum in soils above Lower and Middle Group chromitites of the western Bushveld Complex South Africa. *South African Journal of Geology*, 120(4), 511–524. Available from: https://doi.org/10.25131/gssajg.120.4.511

Pain, C.C., Herwanger, J.V., Worthington, M.H. & Oliveira, C.R.D. (2002) Effective multidimensional resistivity inversion using finite-element techniques. *Geophysical Journal International*, 151(3), 710–728.

Park, C.B., Miller, R.D. & Xia, J. (1999) Multi-channel analysis of surface waves (MASW). *Geophysics*, 649, 659–992. Available from: https://doi.org/10.1190/1.1444590

Poulsen, L.H. & Christensen, N.B. (1999) Hydrogeophysical mapping with the transient electromagnetic sounding method. *European Journal of Environmental and Engineering Geophysics*, 3, 201–220.

Preene, M. (2015) Techniques and developments in quarry and surface mine dewatering. In: Proceedings of the 18th extractive industry geology conference 2014 and technical meeting. Witney: Extractive Industry Geology Conferences Ltd, pp. 194–206.

Rucker, D.F., Glaser, D.R., Osborne, T. & Maehl, W.C. (2009) Electrical resistivity characterization of a reclaimed gold mine to delineate acid rock drainage pathways. *Mine Water and the Environment*, 28, 146–157. Available from: https://doi.org/10.1007/s10230-009-0072-x

Salas-Romero, S., Malehmir, A., Snowball, I. & Brodic, B. (2021) Geotechnical site characterisation using multichannel analysis of surface waves: A case study of an area prone to quick-clay landslides in southwest Sweden. *Near Surface Geophysics*, 19, 699–715. Available from: https://doi.org/10.1002/nsg.12173

Scoates, J.S., Wall, C.J., Friedman R.M., Weis, D., Mathez, E.A. & VanTongeren, J.A. (2021) Dating the Bushveld Complex: timing of crystallization, duration of magmatism, and cooling of the World's largest layered intrusions and related rocks. *Journal of Petrology*, 62, egaa107. Available from: https://doi.org/10.1093/petrology/egaa107

Shankar, K.R. (1994) Groundwater exploration. In: Affordable water supply and sanitation 20th WEDC conference, Colombo, Sri Lanka. Loughborough, UK: Water, Engineering and Development Centre, Loughborough University of Technology, pp. 225–228.

Socco, L.V., & Strobbia, C. (2004). Surface-wave method for near-surface characterization: a tutorial. *Near Surface Geophysics*, 2(4), 165–185. Portico. https://doi.org/10.3997/1873-0604.2004015

Straskraba, V. (2014). Some Technical Aspects Of Open Pit Mine Dewatering, Denver, Colorado, USA. Avialable from: https://www.imwa.info/docs/imds_1979/IMDS1979_Straskraba_481.pdf

Telford, W.M., Geldart, L.P. & Sheriff, R.E. (1990) *Applied Geophysics Second Edition*. Cambridge University Press.

Theron, J.J. & van Niekerk, P.L. (1934) The nature and origin of black turf soils. *South African Journal of Science*, 31, 320346.

Titus, R., Wittüser, K. & Walters, B. (2009) Groundwater and mining in the Bushveld Complex [Extended abstracts]. In *Abstracts of the International Mine and Water Conference*, pp. 178–294.

Tryggvason, A., Rögnvaldsson, S.T. & Flóvenz, Ó.G. (2002) Three-dimensional imaging of the P- and S-wave velocity structure and earthquake locations beneath Southwest Iceland. *Geophysical Journal International*, 151, 848–866. http://doi.org/10.1046/j.1365-246X.2002.01812.x

Twidale, C.R. & Romani, J.R.V. (2005) *Landforms and geology of granite terrains*. London, United Kingdom: Taylor & Francis Group.

United States Geological Survey (USGS). (2023) *Mineral commodity summaries 2023*. Reston: U.S. Geological Survey. Available from: https://doi.org/10.3133/mcs2023

Van Wyk, E. (2013) Southern African pre-Cretaceous deep groundwater flow regimes: evidence and drivers. *13th Biennial Ground Water Division Conference & Exhibition*. Durban: Geological Society of South Africa GroundwaterDivision. 1–15.

Wilson, A.H., Jermy, C.A. & Ridgeway, M. (2005) Rock strength and physical properties of norites of the Merensky and Bastard Units, western Bushveld Complex. *Geological Society of South Africa*, 108, 525–540.

Xia, J., Miller, R.D. & Park, C.B. (1999) Estimation of near-surface shear-wave velocity by inversion of Rayleigh waves. *Geophysics*, 64, 691–700.

Zhang, J. & Toksoz, M.N. (1998) Nonlinear refraction traveltime tomography. *Geophysics*, 63, 1726–1737. Available from: https://doi.org/10.1190/1.1444468

Zientek, M.L., Douglas Causey, J., Parks, H.L. & Miller, R.J. (2014) *Platinum-group elements in Southern Africa-mineral inventory and an assessment of undiscovered mineral resources*. [Scientific Investigations Report 2010–5090–Q, 010, 2010]. Reston, VA, USA: U.S. Geological Survey.

How to cite this article: Gomo, S., Mutshafa, N., Dildar, J., Manzi, M.S.D., Bourdeau, J.E., Brodic, B. et al. (2024) Integration of ground geophysical methods to characterize near-surface aquifer zones within an active mine. *Near Surface Geophysics*, 22, 521–538. https://doi.org/10.1002/nsg.12314